Department of Physics and Astronomy
Heidelberg University

Bachelor Thesis in Physics
submitted by

Fabian Linsenmeier

born in Munich (Germany)

2022

Measurement of the branching fraction for $D^0 \to K^-\pi^+ \left[e^+e^-\right]_{\rho,\omega}$

This Bachelor Thesis has been carried out by Fabian Linsenmeier at the
Physikalisches Institut Heidelberg
under the supervision of
Prof. Dr. Ulrich Uwer

Abstract

This thesis presents the first study of the semileptonic charm decay $D^0 \to K^-\pi^+e^+e^-$ with data from the LHCb experiment at CERN. The analysis uses events from 2017 and 2018 taken at a centre of mass energy of 13 TeV with an integrated luminosity of 3.8 fb^{-1}. It is restricted to the kinematic range 675 MeV/c^2 < m(e^+e^-) < 875 MeV/c^2 where the decay is expected to be dominated by intermediate resonance states ρ^0 and ω. The branching fraction is evaluated relative to the hadronic decay $D^0 \to K^-\pi^+\pi^+\pi^-$ and measured to be:

$$\mathcal{BR}_{D^0 \to K^-\pi^+ [e^+e^-]_{\rho,\omega}} = (26.5 \pm 2.4(\text{stat.}) \pm 0.6(\text{syst.})) \times 10^{-7}$$

The first error is statistical, the second due to systematic uncertainties. Due to the limited scope of the thesis not all systematic error sources were considered. The result is in agreement with previous measurements at other experiments.

Zusammenfassung

Diese Arbeit präsentiert die erste Berechnung einer Zerfallshäufigkeit für den semileptonischen Charm-Zerfall $D^0 \to K^-\pi^+e^+e^-$ mit Daten vom LHCb Experiment am CERN. Es werden Daten aus den Jahren 2017 und 2018 mit einer integrierten Luminosität von 3.8 fb^{-1} verwendet. Die Analyse beschränkt sich auf den kinematischen Bereich 675 MeV/c^2 < m(e^+e^-) < 875 MeV/c^2, in welchem der Zerfall von ρ^0 und ω Resonanzen dominiert wird. Die Zerfallshäufigkeit wird relativ zum hadronischen Zerfall $D^0 \to K^-\pi^+\pi^+\pi^-$ bestimmt:

$$\mathcal{BR}_{D^0 \to K^-\pi^+ [e^+e^-]_{\rho,\omega}} = (26.5 \pm 2.4(\text{stat.}) \pm 0.6(\text{syst.})) \times 10^{-7}$$

Hierbei ist der erste Fehler statistisch, der zweite Fehler beschreibt systematische Unsicherheiten. Aus zeitlichen Gründen konnten nicht alle systematischen Fehlerursachen berücksichtigt werden. Das gemessene Ergebnis stimmt mit bisherigen Messungen von anderen Experimenten überein.

Contents

Chapter 1

Introduction

Despite its great success, the Standard Model of particle physics has failed to answer some of the unsolved questions in physics. So far, there has not been a proper explanation what dark matter is composed of or why there is such a big asymmetry between matter and antimatter in the universe. Therefore, physicists are constantly looking for physics beyond the current model.

Indications for New Physics are searched for in the study of rare charm decays where deviations from the Standard Model could potentially be seen in the test of angular asymmetries or measurements of lepton universality [1, 2]. Promising candidates are the semileptonic decays $D^0 \to h^-h^+l^+l^-$ where $h = K, \pi$ and $l = \mu, e$ denote hadrons and leptons, respectively. Until now, these decay modes have only been observed for muon end states with a measured branching fraction in the order $\mathcal{O}\left(10^{-7}\right)$ [3]. However, the decay modes $D^0 \to h^-h^+e^+e^-$ are expected to be within the reach of the LHCb experiment in the near future [4]. The less suppressed[1] decay $D^0 \to K^-\pi^+e^+e^-$ serves as an excellent reference mode in the search for these decays because of their similar topology.

This study aims to calculate the branching fraction for the decay $D^0 \to K^-\pi^+\left[e^+e^-\right]_{\rho,\omega}$ in the kinematic range $675\,\mathrm{MeV/c^2} < \mathrm{m(e^+e^-)} < 875\,\mathrm{MeV/c^2}$ using data from the LHCb experiment at CERN. In this kinematic range, the decay is expected to be dominated by the intermediate resonance states ρ^0 and ω. While other experiments have seen the decay [5], its branching fraction has not yet been measured at LHCb. A similar analysis, however, was performed by the LHCb collaboration measuring the branching fraction for $D^0 \to K^-\pi^+\left[\mu^+\mu^-\right]_{\rho,\omega}$ in the same kinematic range [6]. While the event selections are very different, one expects - within the context of the Standard Model - to measure the same branching fraction for both decays[2].

For this analysis, D^0 candidates are chosen from the decay of a $D^{*\pm}$-meson via $D^{*\pm} \to D^0\,\pi^\pm$. After applying a cut-based event selection, yields for the signal channel $D^0 \to K^-\pi^+\left[e^+e^-\right]_{\rho,\omega}$ and the normalization mode $D^0 \to K^-\pi^+\pi^+\pi^-$ are determined in simultaneous fits to the D^0 mass distribution. Corresponding efficiencies are calculated using Monte Carlo simulation samples after which a value for the branching fraction can be computed.

The structure of this thesis will be as follows: The next chapter provides the necessary theoretical framework including a quick overview over the Standard Model of particle physics in its current form. After Chapter 3, which will focus on the LHCb experiment and its detector, the actual analysis starts with the event selection

[1] The decay is expected to be in the order $\mathcal{O}\left(10^{-6}\right)$ [5]

[2] Excluding corrections due to different phase spaces

in Chapter 4. This is followed up by Chapter 5 which contains efficiency studies, a description of the fitting process and the calculation of the branching fraction. Final conclusions will be drawn in Chapter 6.

Chapter 2

Theory

2.1 The Standard Model

This section provides an overview over the Standard Model of particle physics in its current form. A detailed introduction to this topic can be found in [7].

During the early 20th century, the understanding of physics underwent drastic changes. The idea of quantum mechanics provided new insights into the world of subatomic physics. Among these was the prediction [8] of the positron and its discovery a couple of years later [9], which marked the first documented discovery of an antiparticle. In the centuries afterwards, many more elementary particles and their antiparticles were discovered. Using the mathematical description of Quantum Field Theory, the **Standard Model** was formulated to put the newly discovered particles into a theoretical framework. The Standard Model is illustrated in Figure 2.1. In its current form, it contains all the elementary particles and three of the fundamental forces known to date. Within the Standard Model, particles can be categorized by their spin value and by the forces they are subject to.

2.1.1 Fundamental forces

The Standard Model successfully describes three of the four **fundamental forces** or **fundamental interactions**. These are the weak, strong and electromagnetic interaction which are all mediated by a class of particles called **gauge bosons**. Not included in the Standard Model is gravity which is the fourth fundamental interaction known to date.

The most well-known force is the **electromagnetic interaction** which is responsible for all electric and magnetic phenomena like electricity, radiowaves or compasses. All particles with electric charge, like protons or electrons, are subject to the electromagnetic force. It is mediated by the photon which itself does not carry electric charge. Since the photon is a massless particle, the electromagnetic force is the only interaction of the Standard Model to have infinite range.

The force-carriers of the **weak interaction**, the $W^{\pm}$- and Z^0-bosons, are massive particles with masses around 80 GeV/c^2 and 91 GeV/c^2 [11]. An example for processes mediated by weak interaction are radioactive $\beta^{\pm}$-decays. Furthermore, the weak force is the only interaction that does not conserve quark flavors. Since the decay studied in this analysis involves a change of the charm quantum number $|\Delta C| = 1$, it can only happen via

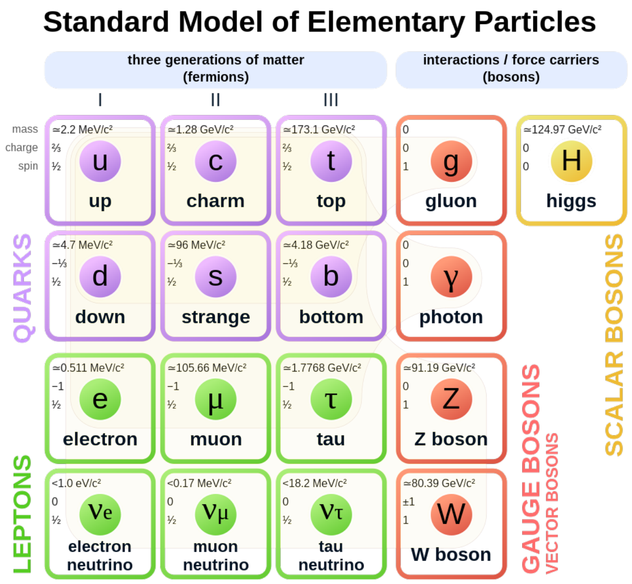

Figure 2.1: Standard Model of particle physics. Taken from [10]

weak interaction. In a process called electroweak unification, physicists were able to show that during the very early stages of the universe, the weak and electromagnetic force were once unified. The unified theory became known as electroweak theory.

The last of three forces to be properly characterized was the **strong interaction**. It is described by quantum chromodynamics (QCD). In contrast to the other interactions, there are three types of charges. They are called colour charges and named red, green and blue. This, however, only serves as a visualization as there is no direct relation to our visual conception of colour. All particles carrying colour charge participate in strong interactions. Eight types of gluons serve as force carriers for the strong force. The gluons mediate between different quarks and are responsible for keeping together multi-quark particles like protons or neutrons. Therefore, the strong interaction is also the force keeping together atomic nuclei. It has been postulated that, at very high energies, the strong force could also be unified with the other two interactions. This, however, is yet to be proven.

2.1.2 Bosons

Bosons are particles with integer spins. Therefore, they obey Bose-Einstein-statistics. The above-mentioned gauge bosons of the fundamental interactions are all bosons with integer spin values. However, the Standard Model knows one more boson, the Higgs particle. It was the last particle of the Standard Model to be observed when it was first detected in 2012 at the Large Hadron Collider in Switzerland [12].

2.1.3 Fermions

Fermions, on the other hand, have half-integer spin values and thus obey Fermi-Dirac statistics. They represent the building blocks of all known matter. The elementary fermions can be split into three generations of leptons and quarks. To each of the following fermions, there exists an antiparticle with the same mass but opposite charge-like quantum numbers.

The three **lepton** generations are also called lepton families. Each family is named after an electron-like particle with electric charge e, i.e. electron, muon or tau lepton. Additionally, every lepton family contains an

Meson type	Quark structure	Invariant mass [MeV/c^2]
π^+	$\overline{d}u$	140
π^-	$d\overline{u}$	140
K^-	$s\overline{u}$	494
D^0	$c\overline{u}$	1865
D^{*+}	$c\overline{d}$	2010
D^{*-}	$\overline{c}d$	2010

Table 2.1: Quark composition and invariant mass for several important mesons. Values are taken from [11]

electrically neutral particle, the neutrino. Neutrinos have long been thought to be massless. In recent years, however, there has been strong experimental evidence for massive neutrinos and precision measurements of the neutrino masses are in progress [13]. All leptons interact weakly and charged leptons (electrons, muons, taus, and their antiparticles) are also subject to electromagnetic interaction.

The non-leptonic, fundamental fermions are called **quarks**. Quarks are constituents of atomic nuclei and subject to both the electroweak and the strong force. The six quarks are called up, down, strange, charm, beauty and top and carry electric charges of either $+\frac{2}{3}e$ or $-\frac{1}{3}e$. Quarks do not exist as free particles. The strong evidence of their existence comes from the investigation of multi-quark particles or **hadrons**. If the hadron carries integer spin, the resulting particle will be a **meson**. For two quarks to form a meson, it must be a combination of a quark and an antiquark $q\overline{q}$ so that the composed particle carries integer electric charge. The lightest known mesons are pions $\pi^{\pm}, \pi^0$ and kaons $K^{\pm}, K_L^0, K_S^0$ which are built of up, down and strange quarks.

2.2 The decay $D^0 \rightarrow K^-\pi^+e^+e^-$

This section introduces the decay mode $D^0 \rightarrow K^-\pi^+e^+e^-$, its particles and some of their key properties.

Charm quarks are quarks of the second generation carrying the same electric charge ($+\frac{2}{3}e$) as an up-quark but with higher rest mass. The lightest known particle to contain a charm quark is the D^0-meson which is unstable and can decay in numerous ways. Oftentimes, it decays into hadronic final states with kaons and pions. Semileptonic decay modes combined make up less than 20 % of all decays [11]. This includes the studied signal mode $D^0 \rightarrow K^-\pi^+e^+e^-$ which is expected to contribute only in the order of 10^{-6} [5]. The signal mode shares some similarities with the hadronic mode $D^0 \rightarrow K^-\pi^+\pi^+\pi^-$: Both decay channels have four-body final states and include a $K^-\pi^+$ pair. Because of the similar topology, $D^0 \rightarrow K^-\pi^+\pi^+\pi^-$ will be used as a normalization mode for this analysis. This will be properly explained in section 2.3.

The D^0 meson candidates for this analysis are reconstructed using the strong decay of a D^* meson. Thus, the full decay mode reads $D^* \rightarrow D^0\,\pi_{slow}$ with $D^0 \rightarrow K^-\pi^+e^+e^-$. Since the mass difference between the D^* and D^0 is very close to the pion rest mass, the pion created in the first decay must carry relatively low momentum. Therefore, it is referenced as π_{slow}. The mass difference $\Delta m = m(D^*) - m(D^0)$ provides an excellent variable to suppress combinatorial background later in the analysis. Figure 2.2 illustrates the full decay tree. Quark compositions and invariant masses for all mentioned mesons are listed in Table 2.1.

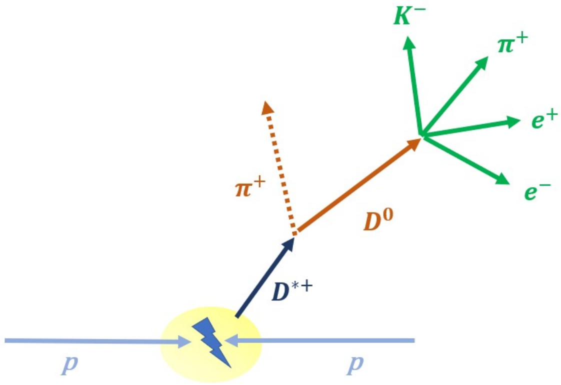

Figure 2.2: Sketch of the full D^{*+} decay tree after the collision. Length and direction of the arrows are arbitrary.

Since the decay $D^0 \to K^-\pi^+e^+e^-$involves a change of the charm quantum number $|\Delta C| = 1$, it can only be mediated by the weak force. The decay is possible either by a direct four-body decay $D^0 \to K^-\pi^+e^+e^-$ or via an intermediate resonant state X which then rapidly decays to two electrons $D^0 \to K^-\pi^+ (X \to e^+e^-)$. Feynman diagrams for both options are shown in Figure 2.3. Since this analysis works inside the invariant mass range of $675\,\mathrm{MeV/c^2} < \mathrm{m_{ee}} < 875\,\mathrm{MeV/c^2}$ of the lepton pair, the resonance states are expected to be ρ^0 or ω mesons [11]. Both ρ^0 and ω are flavorless mesons that can be described as a linear combination of $q\bar{q}$ states.

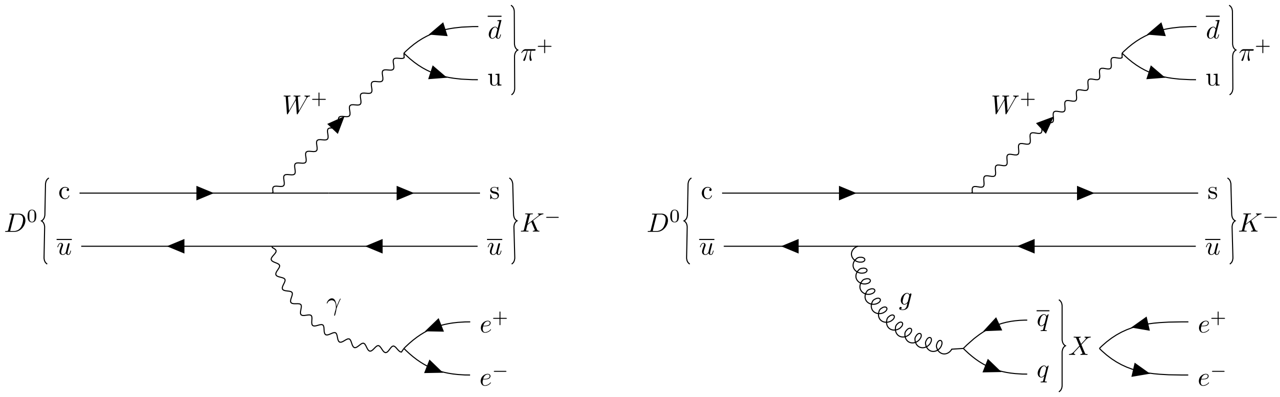

(a) Decay without resonance states

(b) Decay via intermediate resonance X

Figure 2.3: Feynman diagrams regarding different contributions to the signal mode $D^0 \to K^-\pi^+e^+e^-$

An important aspect for decays with electron end states is **bremsstrahlung**. Bremsstrahlung means the loss of energy due to electromagnetic radiation when charged particles interact with matter. It can be explained with the help of electrodynamics. When a negatively charged particle such as an electron flies near an atomic nucleus, it feels the electric field of the positively charged nucleus. Due to this force, the particle is deflected and decelerates. It loses energy which is emitted in form of a photon (see Figure 2.4). While bremsstrahlung is theoretically possible for all charged particles, its rate is inversely proportional to the particle's mass [7]. Therefore, it is particularly prominent for electrons. This will be revisited later.

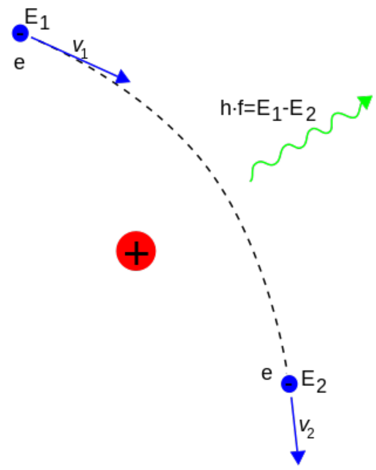

Figure 2.4: Bremsstrahlung radiated by an electron in the electric field of an atomic nucleus. Picture taken from [14]

2.3 Branching fractions and normalization modes

In particle physics, the **branching fraction** or **branching ratio** of a decay mode is the central value for describing its likelihood. It is the fraction with which the mother particles decay via the respective decay channel. For a decay mode A, the branching ratio $\mathcal{B}_A$ can be calculated as:

$$\mathcal{B}_A = \frac{N_A}{N_x} \tag{2.1}$$

Here, N_A stands for the number of decays via decay channel A while N_x represents the total number of decays.

Furthermore, it is necessary to consider the **efficiency** to detect the corresponding channel. To reduce background, restrictions on measured particle properties are applied in the event selection. While these restrictions should mostly reduce background, it will also decrease the signal yield. Therefore, measured yields need to be corrected by the cut efficiencies ϵ. These efficiencies approximate by how much the signal is reduced by the selection. They are defined as:

$$\epsilon = \frac{N_{\text{after}}}{N_{\text{before}}} \tag{2.2}$$

One way of computing branching fractions is with the help of a **normalization mode**. This analysis uses the normalization mode $D^0 \rightarrow K^-\pi^+\pi^+\pi^-$, which shares its mother particle with the signal mode $D^0 \rightarrow K^-\pi^+e^+e^-$. The branching fractions for these two decays are measured relative to each other. Therefore, the factor of total decays N_x will cancel out (see equation 2.1). The following formula will be used:

$$\mathcal{B}_{D^0 \to K^-\pi^+[e^+e^-]_{\rho,\omega}} = \mathcal{B}_{D^0 \,\to\, K^-\pi^+\pi^+\pi^-} \times \frac{\mathcal{N}_{D^0 \to K^-\pi^+[e^+e^-]_{\rho,\omega}}}{\mathcal{N}_{D^0 \,\to\, K^-\pi^+\pi^+\pi^-}} \times \frac{\epsilon_{D^0 \,\to\, K^-\pi^+\pi^+\pi^-}}{\epsilon_{D^0 \to K^-\pi^+[e^+e^-]_{\rho,\omega}}} \tag{2.3}$$

Signal mode quantities $(\epsilon, \mathcal{N}, \mathcal{B})$ are measured inside the ρ^0, ω resonance range only, i.e. $675\,\mathrm{MeV/c^2} < \mathrm{m}(e^+e^-) < 875\ \mathrm{MeV/c^2}$. Normalization mode quantities $(\epsilon, \mathcal{N}, \mathcal{B})$ are measured in the full kinematic range.

Chapter 3

LHCb experiment

All data investigated in this study originates from the LHCb experiment located at the world's largest particle accelerator, the Large Hadron Collider (LHC). This chapter is dedicated to give an overview over the experiment. After introducing the European Organization for Nuclear Research (CERN) and the LHC in section 3.1, section 3.2 will explain the LHCb detector and its components. Important aspects of the data-taking and particle reconstruction are mentioned with a focus on those detector elements that are important for the reconstruction of the signal mode. The last section, 3.3, explains the LHCb's trigger system which is used to identify candidate events.

3.1 CERN and the Large Hadron Collider

Founded shortly after the Second World War, the *European Organization for Nuclear Research*, abbreviated as CERN, has spent the last decades on research in nuclear and particle physics. The organization is located at several sites in Switzerland and France. This area is also the site of CERN's most prestigious project: The **Large Hadron Collider (LHC)**. The LHC [15] is the world's largest particle accelerator with a circumference of more than 26 kilometers. With the help of multiple pre-accelerators, protons are injected into the LHC and accelerated in two separate beam pipes to over 99% the speed of light. At dedicated points, these hadron beams collide creating new particles in the process. Particle detectors of high complexity are built around the collision points to extract information on the collision and its decay products. One of these detectors is the LHCb detector specialized for investigating the decay of heavy mesons containing beauty- or charm-quarks. These are mostly created in gluon-gluon fusion emitted from the colliding quarks.

3.2 LHCb detector

The LHCb detector [16, 17, 18] is a single-arm forward detector. It measures particles that are boosted in beam direction and covers the pseudorapidity range $1.6 < \eta < 4.9$. Figure 3.1 shows the detector layout for Run 2 of the LHC. All components fulfill specific roles in the observation and reconstruction of beauty- and charm-decays. In the following, each detector component will be given a short explanation.

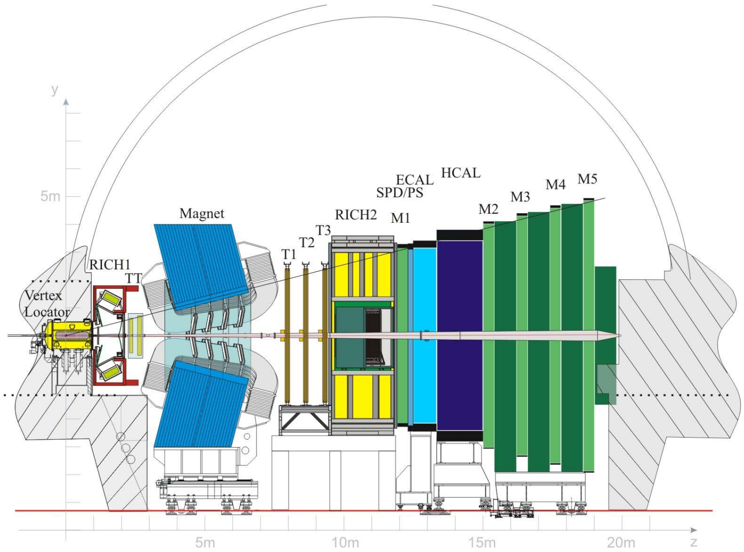

Figure 3.1: Sideview of the LHCb detector for Run 2 of the LHC. Beam direction is from left to right. Taken from [19]

3.2.1 Vertex dectector and tracking

Located directly at the collision point, the **vertex locator** (VELO) is the first detector component to be passed by the particles. The VELO measures the vertices close to the collision point and the distance from tracks to these vertices. Heavy mesons decay very fast and travel only a short distance. Therefore, vertex measurements need to be very precise; a spatial resolution of a few μm is aimed for. Two separate halves consisting of silicon strip sensors make up the VELO. The VELO is constructed in $R - \Phi -$ symmetry. On both sides, there are sensors measuring the azimuthal angle Φ and sensors measuring the radial coordinate R. Since this information is combined with the z-coordinate of the sensor strip, the VELO achieves a complete 3D description of each hit's position.

Four different tracking stations and a dipole magnet are used to reconstruct particle tracks and precisely measure their momenta. Located directly in front of the magnet, the **Tracker Turicensis** (TT) consists of silicon microstrip sensors covering the full LHCb acceptance range. The dipole magnet works at normal temperature and creates a uniform magnetic field in up- or downwards direction with an integrated magnetic field strength of about 4 Tm. Due to the Lorentz force, charged particles are bent by the magnetic field. Behind the magnet, the other three tracking stations (T1-T3) can be found. Since they again measure the track position, combining this information with the TT yields the track curvature caused by the magnet. From this, the particle's momentum can be deduced. The tracking stations T1-T3, however, are built differently compared to the TT. They all consist of an **Inner Tracker** (IT) and **Outer Tracker** (OT) covering different acceptance regions. The inner parts are very similar to the TT as they are also built of silicon strip sensors. The outer parts are gaseous detectors using straw-tubes. These tubes contain gas atoms which are ionized when charged particles pass through. Using high electric voltages, the electrons are accelerated towards the readout anode. The different tracking technologies achieve different spatial resolutions: 50 μm for the TT and IT, 171 μm for the OT [20].

3.2.2 Cherenkov detectors

A key goal for the LHCb detector is particle identification (PID). The different decay products from beauty and charm decays need to be identified with high precision. Typical decay products include protons, pions, kaons, muons, electrons, or photons. Apart from the massless photons, all these particles can be identified by their rest mass. For this, the two **ring-imaging Cherenkov detectors**, RICH-1 and RICH-2, are used. Ring-imaging Cherenkov detectors (RICH) are based on Cherenkov radiation. This electromagnetic radiation is emitted by relativistic particles with velocity v when they pass through matter with refraction index n faster than the speed of light in this medium $c' = c_0/n$. Constructive interference for the radiation waves arises for a fixed angle θ_c. In most cases, this angle can be approximated as:

$$\theta_c = \frac{1}{\beta \cdot \mathrm{n}} \tag{3.1}$$

Therefore, the particle velocity $v = \beta c_0$ can be determined through measurements of the emission angle.

The RICH detectors contain different materials with refraction indices higher than one. When particles pass through the RICH, Cherenkov radiation is emitted under the angle θ_c. This radiation is reflected by spherical mirrors onto photon detectors. Using the position where these signals are detected on the photon detector, θ_c and v (through equation 3.1) can be determined. The RICH combines the velocity with the momentum measured by the magnet spectrometer to deduce a mass hypothesis for the particle.

Since the LHCb detector aims to identify particles in a wide momentum range, PID is achieved by two separate RICH detectors. RICH-1 is located upstream of the magnet and differentiates particles in the range from 1 GeV/c to 60 GeV/c. RICH-2 is located behind the trackers T1-T3 and excels at identifying particles in the momentum range from 15 GeV/c to 100 GeV/c.

3.2.3 Calorimeters and muon chambers

The calorimetric system includes the **scintillating pad detector** (SPD), the **preshower detector** (PS), as well as the **electromagnetic** (ECAL) and **hadronic** (HCAL) **calorimeter** and is located downstream of the RICH-2. It mainly serves two purposes: For one, an energy measurement and PID hypothesis for incoming particles is provided. Furthermore, the hardware trigger L0 (see section 3.3) uses calorimeter signals to trigger on candidate events.

The SPD consists of scintillator pads. Since only charged particles ionize when passing through the scintillator, the SPD can be used to distinguish between photons and electrons. Meanwhile, a lead absorber and another scintillator directly behind it make up the PS. Its main goal is to distinguish between charged electrons and pions. A *shashlik* structure is used for the ECAL: Scintillator planes are separated by lead plates. The incoming electrons and photons interact with matter mostly via bremsstrahlung and pair production. This causes an electromagnetic shower where more and more particles are created and later absorbed. The shape of the shower provides particle identification while the total number of shower particles gives an energy estimation. The ECAL's energy resolution is especially good in regions of high energy, where its resolution surpasses for electrons the momentum resolution of the magnet system. Located behind the ECAL, the HCAL aims to identify hadrons via the detection of hadronic showers. This information is often used in combination with the ECAL to separate electrons from charged pions since only pions will cause a hadronic shower in the HCAL. The last detector parts are the **muon chambers** (M1-M5) which trigger and identify muons. Since muon final states are not of further importance for the analysis, this will not be described in detail.

3.3 LHCb trigger system

Because of storage and bandwidth limitations, not every event in the detector can be saved. To filter out interesting beauty- or charm-events, the LHCb detector uses a trigger system [21] composed of a first-level hardware trigger (L0) and two higher-level software triggers (HLT1 and HLT2).

The **L0** extracts measurements from the calorimeters and muon chambers. In a short processing time of 4μs, the information of SPD/PDS, HCAL and ECAL is used to build an electron, photon or hadron candidate. In a similar process, the muon system builds a muon or dimuon candidate. If no candidate with large transverse momentum p_T is found, the event is discarded. This procedure reduces the full event rate of 40 MHz to about 1 MHz after the L0. The remaining candidate events are passed on to the HLT1.

The **HLT1** works at a software level. Using information from the VELO and the tracking modules, tracks for charged particles with high p_T are partially reconstructed. From this, the algorithm determines the position of the primary vertex (PV). For analysis, tracks with displacement from the PV are far more interesting because the displacement raises the probability that tracks originate from a secondary vertex corresponding to the decay of a beauty- or charm-meson. The HLT1 selects events with high-quality track fits and a significant displacement from the PV. In total, HLT1 reduces data from 1 MHz to about 80 kHz. After the HLT 1 selection, events are stored on buffer.

Later on, the **HLT2** performs a complete event reconstruction using full information from all detector parts. It repeats the track reconstruction for charged particles but without a constraint on tranverse momentum. Additionally, it reconstructs the trajectories of neutral particles by taking information from the calorimeters. In a final step, the PID from the RICH-detectors is added. After the complete reconstruction, the HLT2 trigger lines select events compatible with selected decays of heavy mesons.

Chapter 4

Event selection

4.1 Event samples

This analysis uses data from the LHCb experiment. The data was recorded in 2017 and 2018 during Run 2 of the LHC corresponding to an integrated luminosity of $3.8\,\mathrm{fb}^{-1}$. After the reconstruction process by the LHCb detector as explained in chapter 3, the stripping line *DstarPromptWithD02HHLLLine* selects data that is relevant for the analysis. Events are selected if they were reconstructed with good fit qualities and fulfill requirements on kinematics and particle identification suited for the signal decay $D^0 \to K^-\pi^+e^+e^-$. The stripping line allows for several HLT2 lines that are compatible with semileptonic charm decays. A list of requirements for the stripping line can be found in the appendix. After applying the stripping line, the data is reconstructed under the assumption of the signal mode $D^0 \to K^-\pi^+e^+e^-$. This marks the starting point for the offline cut selection, which will be the subject of section 4.2. Signal and normalization yields will both be determined from the same data sample. Therefore, the $D^0 \to K^-\pi^+\pi^+\pi^-$ yield will be computed from a data sample where it was wrongly reconstructed as $D^0 \to K^-\pi^+e^+e^-$. That means that two pions of the normalization channel have been wrongly identified as electrons[1]. This will be accounted for by using a specific MC sample (see below).

For cross-checks, efficiency studies and fit models, additional results from Monte Carlo (MC) simulations are used. The simulation software [22] simulates pp-collisions and uses the detector layout to imitate event reconstruction. In this analysis, two separate MC samples will be used:

- The first MC sample stems from the simulation of pp-collisions resulting in a $D^0 \to K^-\pi^+e^+e^-$ decay, which is then reconstructed as $D^0 \to K^-\pi^+e^+e^-$. This MC sample will be used to calculate the efficiencies of the signal mode.
- The second MC sample simulates the decay into $D^0 \to K^-\pi^+\pi^+\pi^-$, which is then wrongly reconstructed as $D^0 \to K^-\pi^+e^+e^-$. Therefore, it imitates how $D^0 \to K^-\pi^+\pi^+\pi^-$ is reconstructed in the data sample. This MC sample will be used to calculate efficiencies for the normalization mode.

Table 4.1 lists the number of events in each sample.

[1] The electron identification criteria are weak at this stage

Sample type	Stripped LHCb data	Monte Carlo: $D^0 \to K\pi ee$	Monte Carlo: $D^0 \to K\pi\pi\pi$
Number of entries	250.112.860	466.988	729.020

Table 4.1: Number of events before the offline selection

4.2 Offline selection

The stripped data sample still includes a large amount of background. To reduce background and filter out signal events, an offline selection is applied. All applied restrictions are listed in Table 4.2 at the end of this chapter. In the following, the important cuts from the offline selection will be explained. The offline selection is performed using the ROOT framework [23]. The selection criteria for $D^0 \to K^-\pi^+e^+e^-$ and $D^0 \to K^-\pi^+\pi^+\pi^-$ are kept as similar as possible to reduce systematic uncertainties.

4.2.1 Preselection

First, requirements on the **trigger lines** are imposed. As mentioned in section 3.3, the hardware trigger L0 uses information from the calorimetric system. If the deposited energy surpasses the trigger threshold, the event is kept. Candidates for this analysis need to have triggered on the K, π, or one of the electrons. If the trigger decision was due to another particle, like a muon, the event is not kept. At the HLT1-level, the trigger line *TrackMVA* or *TwoTrackMVA* is required. These lines use a multi-dimensional classifier, the MVA, to determine one displaced track (TrackMVA) or two tracks whose reconstructed decay vertex is displaced (TwoTrackMVA). At the HLT2-level, events are selected if the dedicated HLT2-line *Hlt2RareCharmD02KPieeDecision* has triggered. This line checks the fit qualities, applies kinematic cuts and requires displacements from the primary vertex (PV). A list of the requirements for the HLT2 line can be found in the appendix.

Furthermore, a strict cut is applied to the **delta mass** $\Delta m = m\left(D^0\right) - m\left(D^*\right)$. To be kept, candidates have to lie within the range of $(145.5 \pm 1.8)\,\mathrm{MeV/c^2}$, which is equivalent to the mean and one standard deviation using a Gaussian fit. Applying this cut removes a significant amount of combinatorial background.

In addition to that, candidates are identified by looking for tracks with significant displacement from the primary vertex. This displacement can be measured by the **impact parameter (IP)**. For each particle, the IP measures the perpendicular distance between track and PV. The impact parameter is divided by the fit quality χ^2 if the track was fitted with an origin at the PV. The D^0 daughter particles, namely K, π and e^+e^-, must have values for IP_{χ^2} significantly larger than zero. The D^0 itself, however, is required to have a small IP_{χ^2}.

Stemming from detector noise or wrongly combined detector hits, tracks that were reconstructed by the algorithms can be **ghost tracks**. This means that there was no particle in the first place and the reconstructed track corresponds to a ghost particle. To account for this, the tracking detectors use the detailed hit patterns to compute a **ghost probability** for each track. Events are discarded if one of the long-range particles ($\pi_{slow}, K, \pi, e^+, e^-$) has a ghost probability higher than 20%.

As mentioned in section 3.2, four detector parts provide **particle identitication** for charged particles: The RICH, ECAL, HCAL and muon chambers. For this analysis, PID variables called *ProbNN* are used [24, 25]. These variables are calculated by the classifier ANNPID. For all reconstructed particles, this classifier deduces a likelihood for each of the following particle types: Kaon, pion, proton, electron and muon. Using information from relevant sub-detectors, the classifier gives an output value between 0 and 1. Candidates are identified if

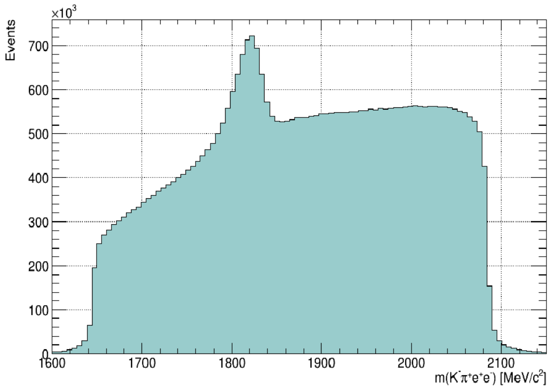

(a) Data before the offline selection

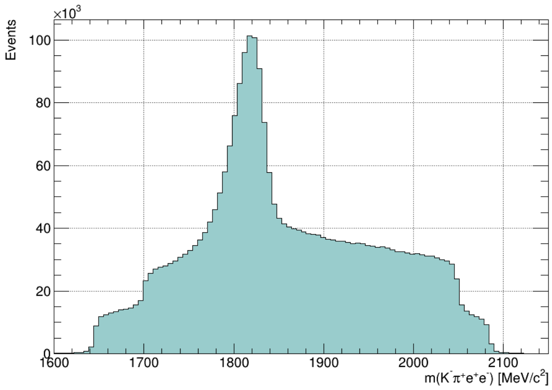

(b) Requirements on the trigger lines applied

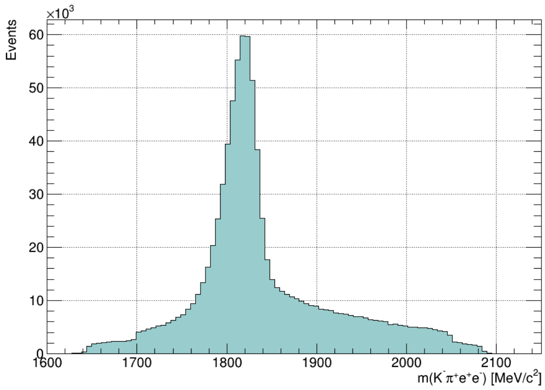

(c) Additional cut on Δm applied

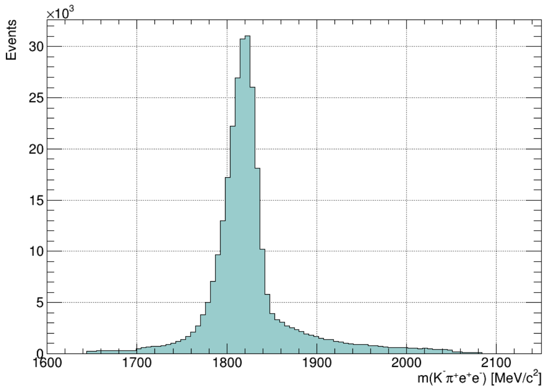

(d) Full preselection applied

Figure 4.1: Comparison of the m($K\pi ee$) distribution at several points during the offline selection. Going from a) to d), additional cuts are applied in each step.

the reconstructed K and π have probabilities higher than 60%.

More restrictions regarding kinematics and fit qualities are applied on the reconstructed D^0, D^* and π_{slow}. These can be found in Table 4.2. For the signal mode $D^0 \to K^-\pi^+e^+e^-$, a significant physical background is expected from $D^0 \to K^-\pi^+\pi^+\pi^-$. This requires two pions to be misidentified as electrons. Nevertheless, this background is relevant since it decays with a branching fraction four orders of magnitude larger than the signal mode [11]. Since the reconstruction used an electron mass hypothesis, the misidentified background peaks between 1820 MeVc^2 and 1830 MeV/c^2, whereas the actual D^0 mass lies at around 1864 MeV/c^2 [11]. Figure 4.1 shows the $m\,(K\pi ee)$ distribution at several points during the offline selection. A lot of the combinatorial background has been successfully suppressed. Nevertheless, the signal is still dominated by the $D^0 \to K^-\pi^+\pi^+\pi^-$ background peaking at 1825 MeV/c^2. At the expected mass of 1864 MeV/c^2, no signal peak can be seen as it is covered by the background tail.

4.2.2 Final selection

To filter out signal against misidentified background, the variable ProbNNe (ProbNN for electron) is used to require a threshold for the electron probability. Figure 4.2 shows the effect of different ProbNNe requirements.

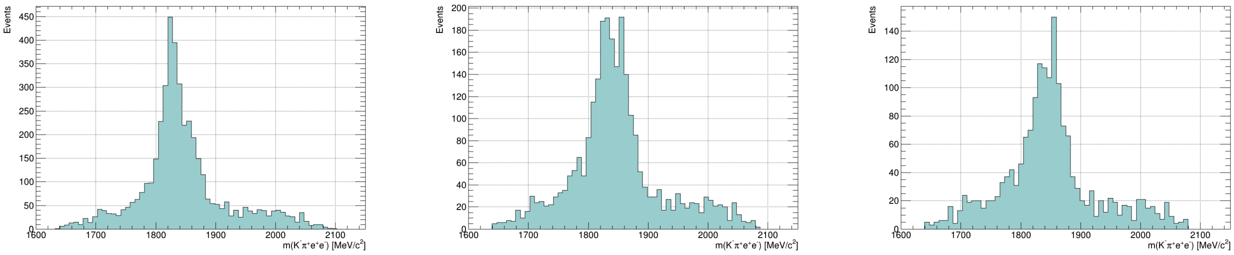

(a) ProbNNE $>$ 20% (b) ProbNNE $>$ 40% (c) ProbNNE $>$ 60%

Figure 4.2: Comparison of the m($K\pi ee$) distribution for several values of ProbNNe. For all three diagrams, the same preselection from figure 4.1d is applied.

As expected, the signal peak at the D^0 mass value becomes visible for higher PID thresholds.

As explained in section 2.2, electrons often radiate bremsstrahlung when passing through matter. If this process happens before electrons have passed all detector parts, these electrons will be measured with too little energy. To account for this, an algorithm is used that checks if a photon was detected in the calorimetric system simultaneously with the electron. If so, that photon's energy is added to the electron energy. However, this method is not perfect: A detected photon might be incorrectly associated with an electron resulting in wrongly added energy. It is also possible that the bremsstrahlung photon is not detected in the calorimetric system and the electron is reconstructed with too little energy.

Therefore, the shapes of mass distributions for events with and without added bremsstrahlung can differ significantly. To account for this, a new variable, the **BremMultiplicity**, is created. The BremMultiplicity is defined as the sum of added photons for both electrons. This variable, however, is not used to discard events. Instead, events are split into two categories, called **Brem0** and **Brem1+**. These correspond to no photon added and at least one photon added, respectively. In the following, the two categories are treated as two exclusive event samples. Since pions do not emit bremsstrahlung, they can only be wrongly associated with photons. Thus, category Brem1+ is expected to contain significantly less background from $D^0 \to K\pi\pi\pi$. Figure 4.3 compares the shape of the mass distribution for both bremsstrahlung categories. Brem0 contains a broad peak ranging from 1820 MeV/c^2 to 1860 MeV/c^2. The Brem1+ distribution peaks much closer to the value of the D^0 mass corresponding to a higher ratio of signal to misidentified background.

To find the optimal value for the ProbNNe variable, a **figure of merit (FOM)** is used. The FOM is defined as:

$$FOM = \frac{N_{signal}}{\sqrt{N_{signal} + N_{background}}} \tag{4.1}$$

For several ProbNNe values ranging from 10% to 80%, the FOM is determined using the fit model as explained in Chapter 5. $N_{\text{background}}$ is the sum of combinatorial and misidentified background. FOMs are calculated separately for Brem0 and Brem1+. The results can be found in the appendix (see Table 6.1). The Brem1+ category achieves a high FOM for all values. Therefore, the selection is optimized by choosing the ProbNNe requirement with the highest FOM for the Brem0 category. The best value is found for a threshold of ProbNNe $>$ 60%.

In Chapter 5, the event selection from this chapter will be used. There are, however, differences between the selections for signal and normalization, respectively. The events for the signal yield include a cut on $m(e^+e^-)$

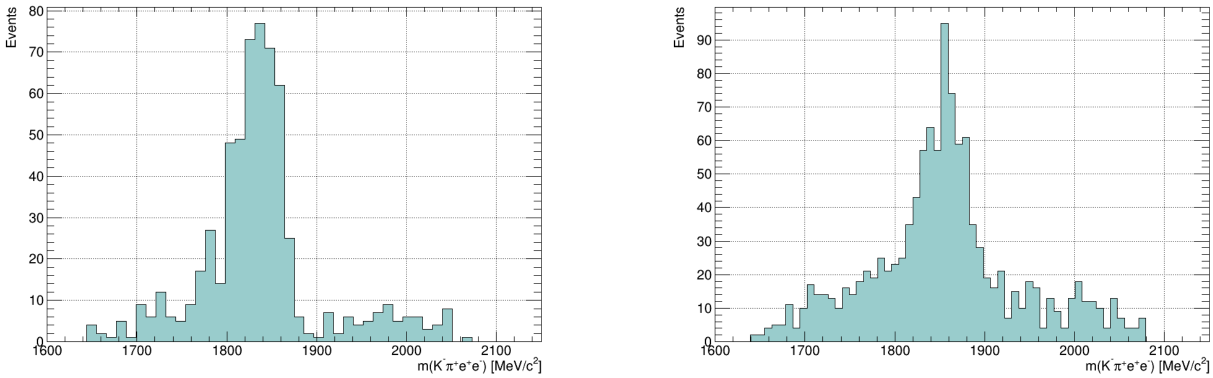

(a) Mass distribution for events from category Brem0 where no photon was added.

(b) Mass distribution for events from category Brem1+ where at least one photon was added.

Figure 4.3: Comparison of m($K\pi ee$) distributions for Brem0 and Brem1+. For both diagrams, the final selection for signal yield is applied (see table 4.2).

whereas the normalization yield uses events from the full kinematic range. In addition to that, the ProbNNe threshold is not required for normalization events. Table 4.2 summarizes the event selection.

Category	**Variable**	**Requirement**
Stripping line	-	*DstarPromptWithD02HHLLLine*
Kinematic range	$m\,(e^{+}e^{-})$	675 - 875 MeV/c^2
Trigger	L0	Hadron or electron (TOS)
	HLT 1	*TrackMVA* or *TwoTrackMVA*
	HLT 2	*Hlt2RareCharmD02KPieeDecision*
Delta mass	Δm	143.7 - 147.3 MeV/c^2
K, π, e	IP_{χ^2}	> 9
	Track: Ghost probability	$< 20\%$
	K: ProbNN kaon	$> 60\%$
	π: ProbNN pion	$> 60\%$
	e: ProbNN electron	$> 60\%$
D^0	p	$>$ 3.000 MeV/c
	p_T	$>$ 2.500 MeV/c
	IP_{χ^2}	< 10
	Vertex fit χ^2 / d.o.f.	< 10
π_{slow}	Track: Ghost probability	$< 20\%$
D^*	p_T	$>$ 2.000 MeV/c
	Vertex fit χ^2 / d.o.f.	< 20
	Cone: p_T - asymmetry	$> (-0.4)$
	Decay tree fit χ^2	> 0
	Number of primary vertices	> 0

Table 4.2: List of all selection requirements. Variables in red are only applied to events used for the signal yield.

Chapter 5

Determining the branching fraction

This chapter is dedicated to fulfill the goal of the analysis and measure the branching fraction for $D^0 \to K^-\pi^+ \left[e^+e^-\right]_{\rho,\omega}$. The next two paragraphs summarize the methods for determining signal and normalization quantities, respectively. Afterwards, sections 5.1 and 5.2 focus on fit results. Corresponding efficiencies will be presented in section 5.3, after which the branching fraction can be calculated in section 5.4. All fits are accomplished as unbinned, maximum likelihood fits using the RooFit package [26] implemented in ROOT.

Signal yields will be calculated from the data sample using events inside the resonance range. This means that a strict cut is applied on the invariant mass of the electron pair. Events are split into the two bremsstrahlung categories, Brem0 and Brem1+. A simultaneous fit is performed to both categories and the $D^0 \to K\pi ee$ yields are added to get the final signal yield. Efficiencies are calculated for both bremsstrahlung categories together[1] using the MC sample which simulates $D^0 \to K^-\pi^+e^+e^-$ decays under $D^0 \to K^-\pi^+e^+e^-$ reconstruction.

Normalization yields will be retrieved from the same data sample. Normalization quantities are determined for the entire kinematic range. Therefore, a new fit is performed with no restriction on the kinematic range. The decay $D^0 \to K^-\pi^+e^+e^-$ is expected to be visible as a peaking background[2]. To make sure that this background is described correctly, events are again split into the two categories Brem0 and Brem1+. Brem0 and Brem1+ are fitted simultaneously, and the $D^0 \to K^-\pi^+\pi^+\pi^-$ yields are added to get the final normalization yield. Efficiencies are determined for both bremsstrahlung categories together using the MC sample, which simulates $D^0 \to K^-\pi^+\pi^+\pi^-$ decays under $D^0 \to K^-\pi^+e^+e^-$ reconstruction. The $D^0 \to K^-\pi^+\pi^+\pi^-$ branching fraction for the entire kinematic range will be taken from [11].

5.1 Fit in resonance range

To determine the signal yield for $D^0 \to K\pi ee$, a fit to the $m\,(K\pi ee)$ distribution inside the resonance range of the electron pair is performed. The complete event selection is applied. This includes the ProbNNe requirement to increase the ratio of signal to misidentified background.

[1] This will be explained in more detail in section 5.3

[2] The lower branching fraction for $D^0 \to K\pi ee$ is expected to be partly compensated by the electron PID cut in the stripping line.

The fit model includes three components:

- $D^0 \to K^-\pi^+e^+e^-$
- $D^0 \to K^-\pi^+\pi^+\pi^-$
- Combinatorial background

The probability density functions (PDFs) used for the $D^0 \to K^-\pi^+e^+e^-$ and $D^0 \to K^-\pi^+\pi^+\pi^-$ shapes are double-sided Crystal Ball functions [27]. They consist of an asymmetric Gaussian with mean m_0 and deviations $\sigma_{L/R}$ but include power-law tails to the left and right. This is chosen since wider and asymmetric tails are expected from too many or too few added photons. Concretely, the Crystal Ball function is defined as follows:

$$CrystalBall(m; m_0, \sigma_L, \sigma_R, \alpha_L, n_L, \alpha_R, n_R) = \begin{cases} A_L \cdot (B_L - \frac{m-m_0}{\sigma_L})^{-n_L}, & \text{for } \frac{m-m_0}{\sigma_L} < -\alpha_L \\ \exp\left(-\frac{1}{2} \cdot \left[\frac{m-m_0}{\sigma_L}\right]^2\right), & \text{for } \frac{m-m_0}{\sigma_L} \leq 0 \\ \exp\left(-\frac{1}{2} \cdot \left[\frac{m-m_0}{\sigma_R}\right]^2\right), & \text{for } \frac{m-m_0}{\sigma_R} \leq \alpha_R \\ A_R \cdot (B_R + \frac{m-m_0}{\sigma_R})^{-n_R}, & \text{otherwise.} \end{cases} \tag{5.1}$$

The normalization factors are:

$$A_i = \left(\frac{n_i}{|\alpha_i|}\right)^{n_i} \cdot \exp\left(-\frac{|\alpha_i|^2}{2}\right) \tag{5.2}$$

$$B_i = \frac{n_i}{|\alpha_i|} - |\alpha_i| \tag{5.3}$$

Both $D^0 \to K^-\pi^+e^+e^-$ and $D^0 \to K^-\pi^+\pi^+\pi^-$ are first fitted to simulation data. The full event selection is applied on the respective MC samples and independent fits are performed to categories Brem0 and Brem1+. Figure 5.1 shows the Monte Carlo fits. In addition to that, residuals [3] are computed to show the difference between data and fit. Residual plots, also referenced as pull plots, are shown below each fit.

After the MC fits, the actual data is fitted. The combinatorial background is approximated by a linear function with slope a. For $D^0 \to K\pi ee$ and $D^0 \to K\pi\pi\pi$, the shape parameters are fixed from the MC fits. All yields and the background slope a are free parameters. Brem0 and Brem1+ are fitted simultaneously, but no parameters are shared between the fits. Figure 5.2 displays the fitted $m\,(K\pi ee)$ distributions and corresponding residual plots. The fit model seems to successfully describe the measured data. Almost all residuals lie within a range of 2σ and no systematic patterns can be detected in the residual plots. The obtained shape parameters and yields for the fit model are listed in Table 5.1.

[3] Residuals σ are defined as $\sigma = \frac{y_{\text{Fit}} - y}{\Delta y}$ with data value y, its error Δy and the fit prediction y_{Fit}

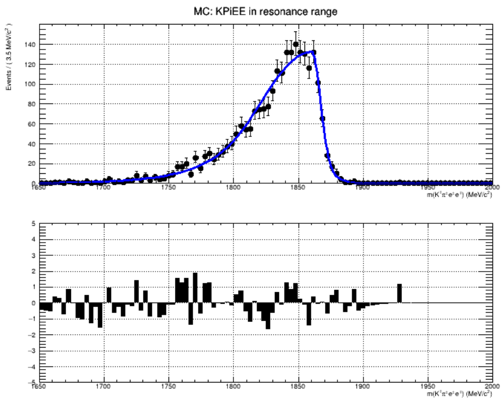

(a) $D^0 \to K^-\pi^+e^+e^-$: Brem0

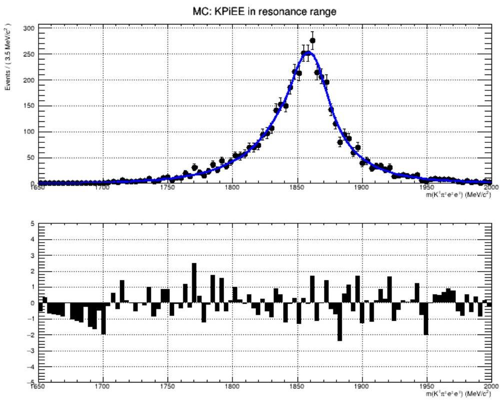

(b) $D^0 \to K^-\pi^+e^+e^-$: Brem1+

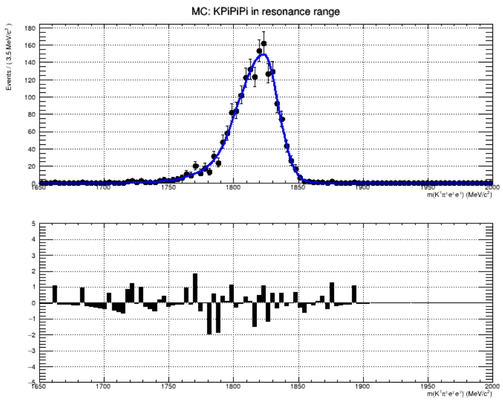

(c) $D^0 \to K^-\pi^+\pi^+\pi^-$: Brem0

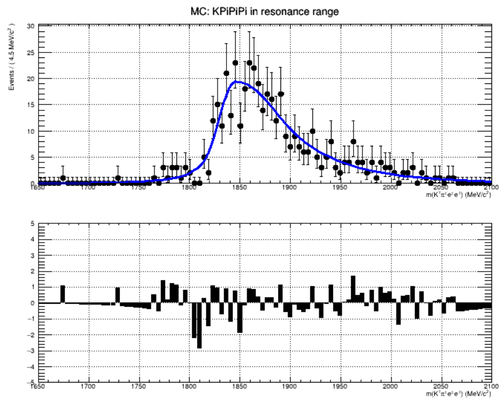

(d) $D^0 \to K^-\pi^+\pi^+\pi^-$: Brem1+

Figure 5.1: Monte Carlo fit results for the resonance range. Four independent fits for $D^0 \to K^-\pi^+e^+e^-$(Brem0 and Brem1+) and $D^0 \to K^-\pi^+\pi^+\pi^-$(Brem0 and Brem1+) are presented. Pull plot below each diagram shows the deviation between data and fit model. All fit parameters are unrestricted.

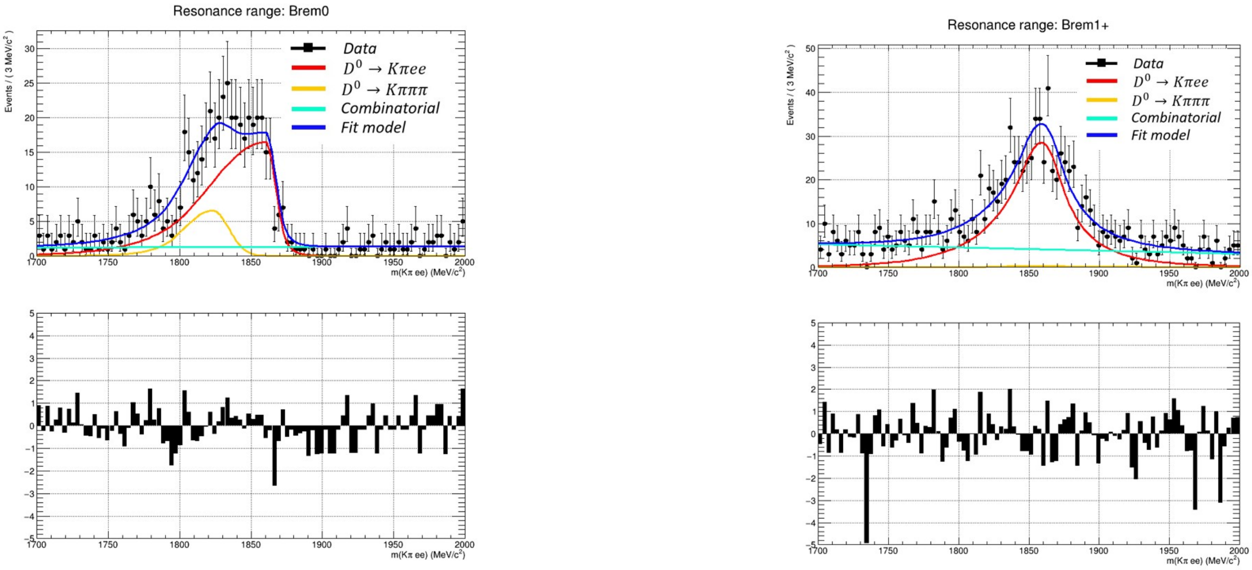

(a) Brem0 (b) Brem1+

Figure 5.2: Data fits inside the resonance range. Individual fit components and the composite fit model are plotted against data. Below each diagram is a pull plot for the composite fit model.

Fit component	Parameter	Value for Brem0	Value for Brem1+
$D^0 \to K^-\pi^+e^+e^-$	m_0	1860.1 ± 1.3	1858.8 ± 1.9
	σ_L	39.8 ± 2.3	18.4 ± 3.5
	σ_R	7.2 ± 1.0	15.8 ± 2.8
	α_L	1.36 ± 0.13	0.65 ± 0.13
	n_L	17.6 ± 3.9	17.5 ± 1.8
	α_R	1.7 ± 0.3	0.84 ± 0.16
	n_R	5.6 ± 3.0	5.0 ± 1.3
	$\mathcal{N}_{D^0\to K\pi ee}$	343 ± 30	601 ± 78
$D^0 \to K^-\pi^+\pi^+\pi^-$	m_0	1823.1 ± 1.1	1846 ± 7
	σ_L	20.1 ± 1.3	17 ± 5
	σ_R	11.3 ± 0.7	48 ± 12
	α_L	1.43 ± 0.16	1.38 ± 0.29
	n_L	7.7 ± 3.5	2.6 ± 1.6
	α_R	2.43 ± 0.26	0.93 ± 0.27
	n_R	3.1 ± 1.6	10 ± 8
	$\mathcal{N}_{D^0\to K\pi\pi\pi}$	91 ± 24	8 ± 229
Combinatorial	a	0.08 ± 0.16	- 0.26 ± 0.13
	$\mathcal{N}_{\text{comb}}$	135 ± 17	416 ± 37

Table 5.1: Summary of the fit results inside the resonance range. For each component, the shape parameters and yields are presented. The uncertainties shown in the table are purely statistical and directly determined by the fit algorithm.

5.2 Fit in full kinematic range

Furthermore, a fit to events in the full kinematic range is performed. The $D^0 \to K^-\pi^+\pi^+\pi^-$ yields from this fit will be used as the normalization yield for calculating the branching fraction. The event selection for this fit excludes the ProbNNe requirement to increase the number of $D^0 \to K^-\pi^+\pi^+\pi^-$ events. Parallel to above, categories Brem0 and Brem1+ are fitted simultaneously with no shared parameters.

The fit is performed to the $m\,(K\pi\pi\pi)$ distribution. This distribution is calculated using a pion mass hypothesis for the two electrons/misidentified pions. This results in a sharper $D^0 \to K^-\pi^+\pi^+\pi^-$ peak. While the mean of the $D^0 \to K^-\pi^+\pi^+\pi^-$ peak is at the D^0 mass value, the $D^0 \to K^-\pi^+e^+e^-$ events now peak at around 1900 MeV/c^2.

In a first step, $D^0 \to K^-\pi^+e^+e^-$ and $D^0 \to K^-\pi^+\pi^+\pi^-$ are fitted to the $m\,(K\pi\pi\pi)$ distribution of simulated MC data using double-sided Crystal Ball functions. The fits are performed to the same event selection used for the data fit. Figure 5.3 shows the results from the MC fits.

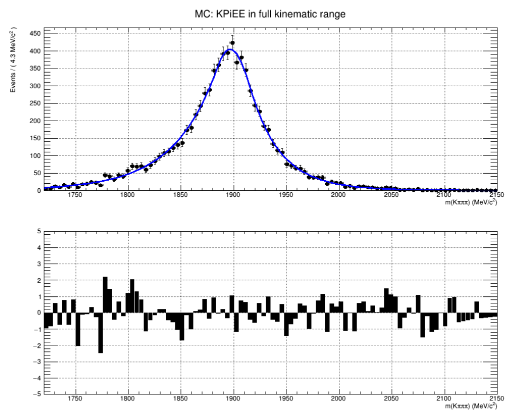

(a) $D^0 \to K^-\pi^+e^+e^-$: Brem0

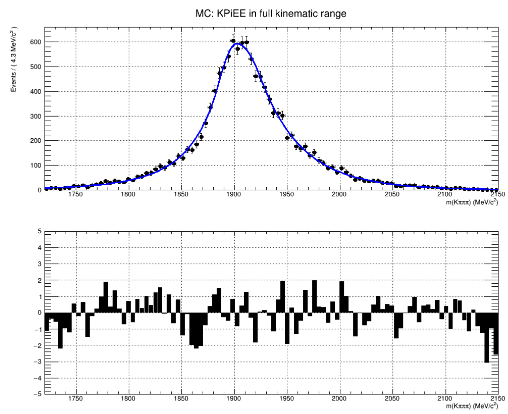

(b) $D^0 \to K^-\pi^+e^+e^-$: Brem1+

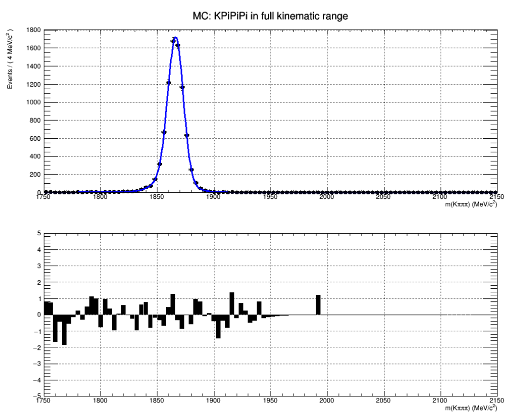

(c) $D^0 \to K^-\pi^+\pi^+\pi^-$: Brem0

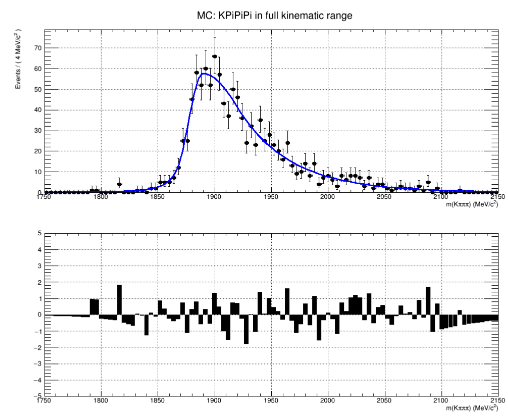

(d) $D^0 \to K^-\pi^+\pi^+\pi^-$: Brem1+

Figure 5.3: Monte Carlo fit results for the full kinematic range. Four independent fits for $D^0 \to K^-\pi^+e^+e^-$(Brem0 and Brem1+) and $D^0 \to K^-\pi^+\pi^+\pi^-$(Brem0 and Brem1+) are presented. Pull plot below each diagram shows the deviation between data and fit model. All fit parameters are unrestricted.

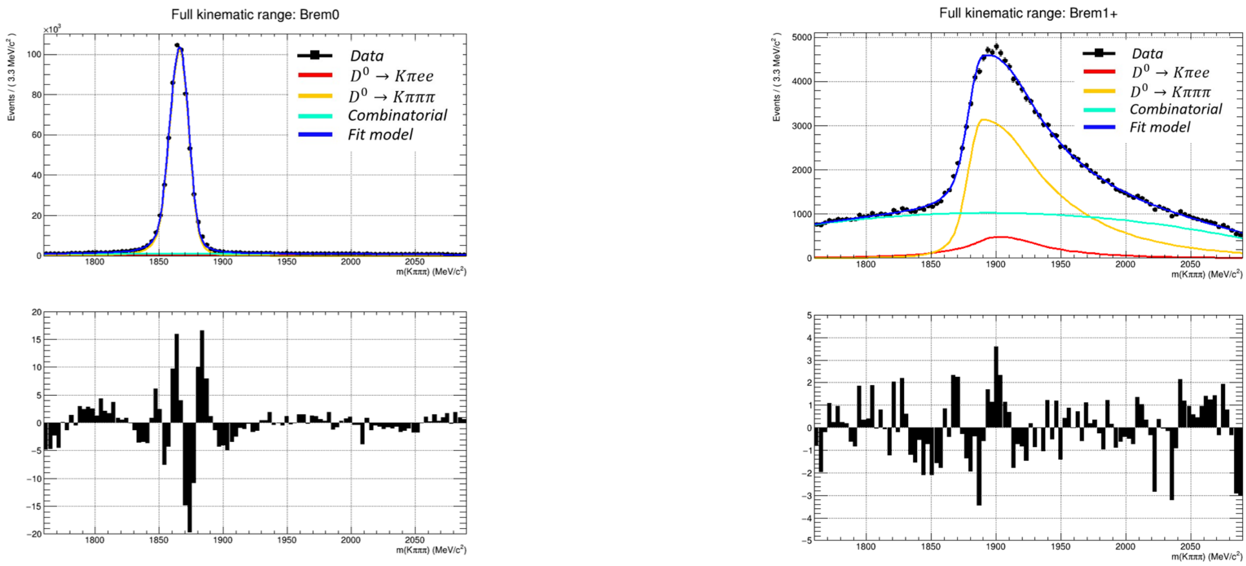

(a) Brem0 (b) Brem1+

Figure 5.4: Data fits in the full kinematic range. Individual fit components and the composite fit model are plotted against data. Below each diagram is a pull plot for the composite fit model. The pull plot for 5.4a is shown with a larger y-axis.

The fit model for the data fit consists of the same components as above. PDF shapes for $D^0 \to K^-\pi^+\pi^+\pi^-$ and $D^0 \to K^-\pi^+e^+e^-$ are fixed from the simulation fits apart from the widths $\sigma_{L/R}$ which are left as free parameters. First, a fit assuming a linear combinatorial background was performed. That fit was not able to describe the combinatorial background properly. Therefore, the combinatorial background is described by a second-order polynomial. A second-order Chebyshev series [28] with parameters a_1 and a_2 is chosen. The series is defined as:

$$Chebyshev(m; a_1, a_2) = T_0(m) + \sum_{n=1}^{2} a_i T_i(m) \tag{5.4}$$

The Chebyshev polynomials T_i are given by:

$$T_0(x) = 1;\ \ T_1(x) = 2x;\ \ T_2(x) = 2x^2 - 1 \tag{5.5}$$

Free parameters for the fit are all yields, the widths for $D^0 \to K^-\pi^+e^+e^-$ and $D^0 \to K^-\pi^+\pi^+\pi^-$ as well as the coefficients for the combinatorial background. Figure 5.4 displays the fits and corresponding pull plots. It should be noted that the fit for Brem0 does not describe the peak perfectly. Several PDF shapes were tried out to improve this, but the Crystal Ball function achieved the best results. To make sure that no background source is missed, the fit was also plotted with a logarithmic axis. This is shown in the appendix (see Figure 6.3). No significant, additional background can be seen.

The range for the data fits in this section was chosen to be restricted to 1760 MeV/c^2 to 2090 MeV/c^2. A larger fit range would have been beneficial for getting a better grasp on the shape of the combinatorial background. However, cuts in the reconstruction regarding the reconstructed D^0 mass lead to sharp cutoffs in data if the fit range is increased. Nevertheless, it needs to be taken into account that the smaller fit range might reduce yields for $D^0 \to K^-\pi^+e^+e^-$ or $D^0 \to K^-\pi^+\pi^+\pi^-$. MC samples are used to determine fit range efficiencies $\epsilon_{Fitrange}$. The parameter $\epsilon_{Fitrange}$ shows how many events lie within the reduced fit range.

Table 5.2 summarizes the obtained parameters for the data fit. In addition to that, $\epsilon_{Fitrange}$ is presented for $D^0 \to K^-\pi^+e^+e^-$ and $D^0 \to K^-\pi^+\pi^+\pi^-$. Furthermore, the table contains $\mathcal{N}_{D^0\to K\pi\pi\pi,\,corr}$ and $\mathcal{N}_{D^0\to K\pi ee,\,corr}$ where the respective yield is corrected with its fit range efficiency.

Fit component	**Parameter**	**Value for Brem0**	**Value for Brem1+**
$D^0 \to K^-\pi^+e^+e^-$	m_0	1896.5 ± 2.0	1902.2 ± 2.4
	σ_L	22.9 ± 4.3	21.6 ± 3.3
	σ_R	24.0 ± 2.7	30.8 ± 3.7
	α_L	0.56 ± 0.11	0.78 ± 0.12
	n_L	34 ± 17	5.1 ± 0.9
	α_R	0.85 ± 0.11	0.781 ± 0.010
	n_R	21 ± 16	21.3 ± 2.2
	$\epsilon_{Fitrange}$	(98.25 ± 0.14)%	(98.54 ± 0.11)%
	$\mathcal{N}_{D^0\to K\pi ee}$	11 638 ± 645	13 191 ± 2806
	$\mathcal{N}_{D^0\,\to\,K\pi ee,\,\mathrm{corr.}}$	11 846 ± 656	13 386 ± 2848
$D^0 \to K^-\pi^+\pi^+\pi^-$	m_0	1866.03 ± 0.29	1889.5 ± 3.4
	σ_L	8.178 ± 0.013	11.47 ± 0.16
	σ_R	7.156 ± 0.012	43.3 ± 0.7
	α_L	1.85 ± 0.09	1.6 ± 0.3
	n_L	2.29 ± 0.25	3.0 ± 1.3
	α_R	1.96 ± 0.11	0.81 ± 0.20
	n_R	4.1 ± 0.7	32 ± 25
	$\epsilon_{Fitrange}$	(99.90 ± 0.03)%	(99.6 ± 0.2)%
	$\mathcal{N}_{D^0\to K\pi\pi\pi}$	622 482 ± 854	80 796 ± 1920
	$\mathcal{N}_{D^0\to K\pi\pi\pi,\,corr.}$	623 105 ± 855	81 121 ± 1928
Combinatorial	a_1	-0.218 ± 0.007	-0.193 ± 0.010
	a_2	-0.245 ± 0.007	-0.252 ± 0.014
	$\mathcal{N}_{\mathrm{comb}}$	99 850 ± 574	87 394 ± 1462

Table 5.2: Summary of the fit results in the full kinematic range. For each component, the shape parameters and yields are presented. Uncertainties shown in the table are purely statistical and directly computed by the fit algorithm.

5.3 Efficiencies

This section describes the calculation of the efficiency ratio in regard to the event selections. The efficiencies are determined using the MC samples specified in 4.1. Efficiencies are determined for both bremsstrahlung categories together and not separately for each category. This works only if the relative number of events with added bremsstrahlung is correctly described by the MC simulation. This assumption is supported by a cross check between MC and data. The relative number of events with at least one added photon ϵ_{Brem}[4] is compared for Monte Carlo and data . Table 5.3 shows the results for the comparison. Since the values for MC and data are compatible, the MC simulation seems to describe the bremsstrahlung fraction correctly.

Decay mode	ϵ_{Brem} (MC) [%]	ϵ_{Brem} (data) [%]
$D^0 \to K^-\pi^+ \left[e^+e^-\right]_{\rho,\omega}$	60.9 $\pm$ 0.3	63.7 $\pm$ 6.1
$D^0 \to K^-\pi^+\pi^+\pi^-$	12.1 $\pm$ 0.3	11.5 $\pm$ 0.4

Table 5.3: Comparison of ϵ_{Brem} for $D^0 \to K^-\pi^+ \left[e^+e^-\right]_{\rho,\omega}$ and $D^0 \to K^-\pi^+\pi^+\pi^-$ in data and Monte Carlo after the selection has been applied. Data values are calculated using the yields stated in Tables 5.1 and 5.2.

The efficiencies for $D^0 \to K^-\pi^+ \left[e^+e^-\right]_{\rho,\omega}$ and $D^0 \to K^-\pi^+\pi^+\pi^-$ are grouped in several selection categories and listed in Table 5.4. The first category, reconstruction, includes geometrical acceptance, filter cuts and the reconstruction as $D^0 \to K^-\pi^+e^+e^-$. It should be noted that this category already includes a slight electron PID cut which explains why the reconstruction efficiency is significantly lower for $D^0 \to K^-\pi^+\pi^+\pi^-$. The efficiency errors presented in the table are due to the limited sample size and are approximated by binomial errors.

Category	$D^0 \to K^-\pi^+ \left[e^+e^-\right]_{\rho,\omega}$	$D^0 \to K^-\pi^+\pi^+\pi^-$
Reconstruction (as $K\pi ee$)	1.17 e-03	1.85 e-05
Trigger	14.8%	14.2%
Δm	82.5%	84.7%
Selection	90.4%	90.3%
Ghost tracks and hadron PID	75.8%	63.7%
ProbNNe	54.9%	1 (not required)
Total	(53.7 $\pm$ 0.6) e-06	(12.93 $\pm$ 0.13) e-07

Table 5.4: Efficiencies for $D^0 \to K^-\pi^+e^+e^-$ [inside resonance range] and $D^0 \to K^-\pi^+\pi^+\pi^-$ [full kinematic range]. The errors shown in the table are only based on the finite size of the MC samples and approximated by a binomial error. The first category, reconstruction, already includes a slight cut on electron PID in the stripping line.

5.4 Final value for branching fraction

In the last sections, signal ($D^0 \to K^-\pi^+ \left[e^+e^-\right]_{\rho,\omega}$) and normalization ($D^0 \to K^-\pi^+\pi^+\pi^-$) yields and their respective efficiency ratio were determined. The results are summarized in Table 5.5.

The branching fraction for the signal mode $D^0 \to K^-\pi^+ \left[e^+e^-\right]_{\rho,\omega}$ is calculated using equation (2.3) together with the results from Table 5.5. The result is:

[4] $\epsilon_{\text{Brem}} = \frac{N(Brem1+)}{N(Brem0)+N(Brem1+)}$

	Signal mode	Normalization mode
Yield $\mathcal{N}$	943 ± 84	704 226 ± 2109
Efficiency ϵ $[10^{-7}]$	537 ± 6	12.93 ± 0.13
$\mathcal{B}_{\text{norm}}$ $[10^{-2}]$	-	8.23 ± 0.14

Table 5.5: Summary of yields and efficiencies for signal and normalization mode. The value for $\mathcal{B}_{D^0 \to K^-\pi^+\pi^+\pi^-}$ is taken from [11].

$$\mathcal{B}_{D^0 \to K^-\pi^+ [e^+e^-]_{\rho,\omega}} = (26.54 \pm 2.37(\mathcal{N}) \pm 0.42(\epsilon) \pm 0.45(\mathcal{B}_{\text{norm}})) \times 10^{-7} \tag{5.6}$$

$$\mathcal{B}_{D^0 \to K^-\pi^+ [e^+e^-]_{\rho,\omega}} = (26.5 \pm 2.4(\text{stat.}) \pm 0.6(\text{syst.})) \times 10^{-7} \tag{5.7}$$

The statistical error stems from the $\mathcal{N}_{D^0 \to K\pi ee}$ and $\mathcal{N}_{D^0 \to K\pi\pi\pi}$ uncertainties. Since they are determined in separate fits, $D^0 \to K\pi ee$ and $D^0 \to K\pi\pi\pi$ yields are considered to be uncorrelated. The second error is systematical and contains two sources: The efficiency error as well as the uncertainty from $\mathcal{B}_{D^0 \to K^-\pi^+\pi^+\pi^-}$. They are quadratically summed since no source for correlation is assumed.

Due to the limited scope of this thesis, several sources for systematic uncertainties were not considered. The relative systematic uncertainty for the measured branching fraction is 2.3%, but is expected to be significantly underestimated. Toy studies should be implemented to test the fit performance and study systematic errors due to the fit model. For instance, there are biases caused by the choice to use double-sided Crystal Ball functions for $D^0 \to K^-\pi^+e^+e^-$ and $D^0 \to K^-\pi^+\pi^+\pi^-$. These biases can be investigated by fitting different PDFs to toy samples. The results can be used to estimate the associated systematic uncertainty. Furthermore, systematic uncertainties for the efficiencies should be studied. This can be done using cross checks between Monte Carlo and data. If all possible error sources are considered, it could potentially bring the relative systematic error to the range of 10%; see for instance the similar analysis by the LHCb collaboration for $D^0 \to K^-\pi^+ [\mu^+\mu-]_{\rho,\omega}$ [6].

Chapter 6

Conclusion

This thesis presents a successful measurement of the semileptonic charm decay $D^0 \to K^-\pi^+e^+e^-$ with data from the LHCb experiment. The analysis was restricted to the kinematic range 675 MeV/c^2 < m(e^+e^-) < 875 MeV/c^2 where the decay is expected to be dominated by ρ^0 and ω resonance states. The branching fraction was measured relative to the hadronic decay $D^0 \to K^-\pi^+\pi^+\pi^-$. Using LHCb data from 2017 and 2018 with an integrated luminosity of 3.8 fb^{-1}, the number of decay events for $D^0 \to K^-\pi^+e^+e^-$ and $D^0 \to K^-\pi^+\pi^+\pi^-$ in the data sample was determined. Simulated Monte Carlo samples were used for fit models and efficiency studies. The branching fraction is measured to be:

$$\mathcal{B}_{D^0 \to K^-\pi^+ [e^+e^-]_{\rho,\omega}} = (26.5 \pm 2.4(\text{stat.}) \pm 0.6(\text{syst.})) \times 10^{-7} \tag{6.1}$$

While the statistical error represents the fluctuations of yields, the systematical error includes uncertainties from the limited sample size of the simulation data as well as the uncertainty of the reference value for $\mathcal{B}_{D^0 \to K^-\pi^+\pi^+\pi^-}$. The measured branching fraction is in accordance ($2.2\,\sigma$) with a previous result from the BaBar experiment [5].

An entire study of systematic uncertainties should be performed to complement the result of this thesis. This includes toy studies regarding the fit model and data-driven methods to investigate the efficiency ratio. Especially for the PID and trigger efficiencies, significant deviations are expected between data and simulation. The analysis could also be improved by using dedicated $D^0 \to K^-\pi^+\pi^+\pi^-$ data and simulation samples. This would have been preferred for this analysis already but had to be discarded because of missing $D^0 \to K\pi\pi\pi$ simulations. Using dedicated $D^0 \to K^-\pi^+\pi^+\pi^-$ samples avoids the misidentified reconstruction for $D^0 \to K^-\pi^+\pi^+\pi^-$ events. This would help to suppress systematic errors since $D^0 \to K^-\pi^+\pi^+\pi^-$ and $D^0 \to K^-\pi^+e^+e^-$ are then reconstructed in a similar way.

Furthermore, it would be a natural next step to investigate the branching fraction for $D^0 \to K^-\pi^+e^+e^-$ in the kinematic regions below 675 MeV/c^2 and above 875 MeV/c^2. This would also be beneficial to the search for the decays $D^0 \to h^+h^-e^+e^-$ since systematic uncertainties are expected to cancel better if signal and normalization mode are investigated in a similar kinematic range.

Bibliography

[1] Hector Gisbert, Marcel Golz, and Dominik Stefan Mitzel. Theoretical and experimental status of rare charm decays. *Modern Physics Letters A*, 36(04):2130002, February 2021.

[2] Luigi Cappiello, Oscar Cata, and Giancarlo D'Ambrosio. Standard Model prediction and new physics tests for $D^0 \to h_1^+ h_2^- l^+ l^-$ ($h = \pi, K; l = e, \mu$). 2012. Publisher: arXiv Version Number: 2.

[3] LHCb collaboration, R. Aaij, et al. Observation of D^0 meson decays to $\pi^+\pi^-\mu^+\mu^-$ and $K^+K^-\mu^+\mu^-$ final states. *Physical Review Letters*, 119(18):181805, October 2017. arXiv:1707.08377 [hep-ex].

[4] LHCb Collaboration, I. Bediaga, et al. Physics case for an LHCb Upgrade II - Opportunities in flavour physics, and beyond, in the HL-LHC era. 2018. Publisher: arXiv Version Number: 4.

[5] J.P. Lees et al. Observation of the Decay $D^0 \to K^-\pi^+e^+e^-$. *Physical Review Letters*, 122(8):081802, February 2019.

[6] LHCb collaboration, R. Aaij, et al. First observation of the decay $D^0 \to K^-\pi^+\mu^+\mu^-$ in the $\rho^0 - \omega$ region of the dimuon mass spectrum. *Physics Letters B*, 757:558–567, June 2016. arXiv:1510.08367 [hep-ex].

[7] Mark Thomson. *Modern Particle Physics:*. Cambridge University Press, 1 edition, September 2013.

[8] Paul Adrien Maurice Dirac and Ralph Howard Fowler. The quantum theory of the electron. *Proceedings of the Royal Society of London. Series A, Containing Papers of a Mathematical and Physical Character*, 117(778):610–624, February 1928. Publisher: Royal Society.

[9] Carl D. Anderson. The Positive Electron. *Physical Review*, 43(6):491–494, March 1933.

[10] The Wikipedia community. Standard model, from Wikipedia, the free encyclopedia.

[11] Particle Data Group, P A Zyla, et al. Review of Particle Physics. *Progress of Theoretical and Experimental Physics*, 2020(8):083C01, August 2020.

[12] G. Aad et al. Observation of a new particle in the search for the Standard Model Higgs boson with the ATLAS detector at the LHC. *Physics Letters B*, 716(1):1–29, 2012.

[13] G. Drexlin, V. Hannen, S. Mertens, and C. Weinheimer. Current Direct Neutrino Mass Experiments. *Advances in High Energy Physics*, 2013:1–39, 2013.

[14] The Wikipedia community. Bremsstrahlung, from Wikipedia, the free encyclopedia.

[15] Michael Hauschild. *Exploring the Large Hadron Collider - CERN and the Accelerators: The World Machine Clearly Explained.* essentials. Springer Fachmedien Wiesbaden, Wiesbaden, 2021.

[16] The LHCb Collaboration et al. The LHCb Detector at the LHC. *Journal of Instrumentation*, 3(08):S08005–S08005, August 2008. Publisher: IOP Publishing.

[17] I. Belyaev, G. Carboni, N. Harnew, C. Matteuzzi, and F. Teubert. The history of LHCb. *The European Physical Journal H*, 46(1):3, March 2021.

[18] Hermann Kolanoski and Norbert Wermes. *Teilchendetektoren*. Springer Berlin Heidelberg, Berlin, Heidelberg, 2016.

[19] Rolf Lindner. LHCb layout_2. LHCb schema_2. February 2008.

[20] P. d'Argent et al. Improved performance of the LHCb outer tracker in LHC run 2. *Journal of Instrumentation*, 12(11):P11016–P11016, nov 2017.

[21] R. Aaij et al. Design and performance of the LHCb trigger and full real-time reconstruction in Run 2 of the LHC. *Journal of Instrumentation*, 14(04):P04013–P04013, April 2019.

[22] S. Agostinelli et al. Geant4—a simulation toolkit. *Nuclear Instruments and Methods in Physics Research Section A: Accelerators, Spectrometers, Detectors and Associated Equipment*, 506(3):250–303, 2003.

[23] I. Antcheva et al. ROOT — A C++ framework for petabyte data storage, statistical analysis and visualization. *Computer Physics Communications*, 180(12):2499–2512, December 2009.

[24] Lucio Anderlini, Sean Benson, Olli Lupton, Barbara Sciascia, and Vladimir Gligorov. Computing strategy for PID calibration samples for LHCb Run 2. Technical report, CERN, Geneva, July 2016.

[25] Roel Aaij et al. Selection and processing of calibration samples to measure the particle identification performance of the LHCb experiment in Run 2. *EPJ Techniques and Instrumentation*, 6(1):1, December 2019.

[26] Wouter Verkerke and David Kirkby. The RooFit toolkit for data modeling. 2003. Publisher: arXiv Version Number: 1.

[27] Tomasz Skwarnicki. *A study of the radiative CASCADE transitions between the Upsilon-Prime and Upsilon resonances*. PhD thesis, Cracow, INP, 1986.

[28] John P Boyd. *Chebyshev and Fourier spectral methods*. Courier Corporation, 2001.

Appendix

ProbNNe higher than	**FOM: Brem0**	**FOM: Brem1+**
10	11.56	21.98
20	12.00	21.89
30	13.02	21.39
40	14.02	20.55
50	14.16	18.90
60	14.37	18.76
70	13.36	18.11
80	12.63	16.96

Table 6.1: Figures of merit for several ProbNNe requirements

Particle	Variable		signal modes 2015-2016	signal modes 2017-2018	normalisation 2015-2016	normalisation 2017-2018
h, μ, e	p	$>$	3 GeV/c	3 GeV/c	3 GeV/c	3 GeV/c
	p_T	$>$	300 MeV/c	300 MeV/c	300 MeV/c	300 MeV/c
	Track χ^2/dof	$<$	4	4	4	4
μ	IP χ^2	$>$	2	2	2	2
e	IP χ^2	$>$	3	3	3	3
$(\ell\ell)$	m$(\ell\ell)$	$<$	2100 MeV/c^2	2100 MeV/c^2	2100 MeV/c^2	2100 MeV/c^2
	$\sum p_T$	$>$	0. MeV/c	0. MeV/c	0. MeV/c	0. MeV/c
	DOCA	$<$	0.1 mm	0.1 mm	0.1 mm	0.1 mm
Dilepton object	FD χ^2	$>$	20	20	9	9
	FD	$>$	0 mm	0 mm	0 mm	0 mm
	$M_{corrected}$	$<$	3500 MeV/c^2	3500 MeV/c^2	3500 MeV/c^2	3500 MeV/c^2
$(hh\ell\ell)$	m$(hh\ell\ell)$	$>$	–	1550 MeV/c^2	–	1550 MeV/c^2
		$<$	2100 MeV/c^2	2200 MeV/c^2	2100 MeV/c^2	2200 MeV/c^2
	max p_T	$>$	0. MeV/c	0. MeV/c	0. MeV/c	0. MeV/c
	$\sum p_T$	$>$	3000 MeV/c	3000 MeV/c	3000 MeV/c	3000 MeV/c
	min DOCA	$<$	0.1 mm	0.2 mm	0.1 mm	0.2 mm
	max DOCA	$<$	0.2 mm	0.3 mm	0.2 mm	0.3 mm
	max IP χ^2	$>$	9	9	9	9
D^0	m(D^0)	$>$	1800 MeV/c^2	1700 MeV/c^2	1800 MeV/c^2	1700 MeV/c^2
		$<$	1950 MeV/c^2	2050 MeV/c^2	1950 MeV/c^2	2050 MeV/c^2
	Vertex χ^2/dof	$<$	15	15	15	15
	$M_{corrected}$	$<$	3500 MeV/c^2	3500 MeV/c^2	3500 MeV/c^2	3500 MeV/c^2
	FD χ^2	$>$	49	49	36	16
	DIRA	$>$	0.9999	0.9999	0.9999	0.9999
	IP χ^2	$<$	25	25	25	25
	$\sum \sqrt{IP\chi^2}$	$>$	12	8	12	8
π_s	p_T	$>$	–	120 MeV/c	–	120 MeV/c
$(D^0\pi_s)$	Q	$>$	–	130 MeV/c^2-m_π	–	130 MeV/c^2-m_π
		$<$	–	180 MeV/c^2-m_π	–	180 MeV/c^2-m_π
D^{*+}	Q	$>$	–	130 MeV/c^2-m_π	–	130 MeV/c^2-m_π
		$<$	–	170 MeV/c^2-m_π	–	170 MeV/c^2-m_π
	Vertex χ^2/dof	$<$	–	25	–	25

Figure 6.1: List of requirements for the stripping line *PromptWithD02HHLLLine*

Particle	Variable		signal modes 2015-2016	signal modes 2017-2018	normalisation 2015-2016	normalisation 2017-2018
h, μ, e	p	$>$	3 GeV/c	3 GeV/c	3 GeV/c	3 GeV/c
	p_T	$>$	300 MeV/c	300 MeV/c	300 MeV/c	300 MeV/c
	Track χ^2/dof	$<$	4	4	4	4
μ	IP χ^2	$>$	2	2	2	2
e	IP χ^2	$>$	3	3	3	3
$(\ell\ell)$	m$(\ell\ell)$	$<$	2100 MeV/c^2	2100 MeV/c^2	2100 MeV/c^2	2100 MeV/c^2
	$\sum p_T$	$>$	0. MeV/c	0. MeV/c	0. MeV/c	0. MeV/c
	DOCA	$<$	0.1 mm	0.1 mm	0.1 mm	0.1 mm
Dilepton object	FD χ^2	$>$	20	20	9	9
	FD	$>$	0 mm	0 mm	0 mm	0 mm
	$M_{corrected}$	$<$	3500 MeV/c^2	3500 MeV/c^2	3500 MeV/c^2	3500 MeV/c^2
$(hh\ell\ell)$	m$(hh\ell\ell)$	$>$	–	1550 MeV/c^2	–	1550 MeV/c^2
		$<$	2100 MeV/c^2	2200 MeV/c^2	2100 MeV/c^2	2200 MeV/c^2
	max p_T	$>$	0. MeV/c	0. MeV/c	0. MeV/c	0. MeV/c
	$\sum p_T$	$>$	3000 MeV/c	3000 MeV/c	3000 MeV/c	3000 MeV/c
	min DOCA	$<$	0.1 mm	0.2 mm	0.1 mm	0.2 mm
	max DOCA	$<$	0.2 mm	0.3 mm	0.2 mm	0.3 mm
	max IP χ^2	$>$	9	9	9	9
D^0	m(D^0)	$>$	1800 MeV/c^2	1700 MeV/c^2	1800 MeV/c^2	1700 MeV/c^2
		$<$	1950 MeV/c^2	2050 MeV/c^2	1950 MeV/c^2	2050 MeV/c^2
	Vertex χ^2/dof	$<$	15	15	15	15
	$M_{corrected}$	$<$	3500 MeV/c^2	3500 MeV/c^2	3500 MeV/c^2	3500 MeV/c^2
	FD χ^2	$>$	49	49	36	16
	DIRA	$>$	0.9999	0.9999	0.9999	0.9999
	IP χ^2	$<$	25	25	25	25
	$\sum \sqrt{IP\chi^2}$	$>$	12	8	12	8
π_s	p_T	$>$	–	120 MeV/c	–	120 MeV/c
$(D^0\pi_s)$	Q	$>$	–	130 MeV/c^2-m_π	–	130 MeV/c^2-m_π
		$<$	–	180 MeV/c^2-m_π	–	180 MeV/c^2-m_π
D^{*+}	Q	$>$	–	130 MeV/c^2-m_π	–	130 MeV/c^2-m_π
		$<$	–	170 MeV/c^2-m_π	–	170 MeV/c^2-m_π
	Vertex χ^2/dof	$<$	–	25	–	25

Figure 6.2: List of requirements to trigger the HLT2 selection *Hlt2RareCharmD02KPieeDecision*

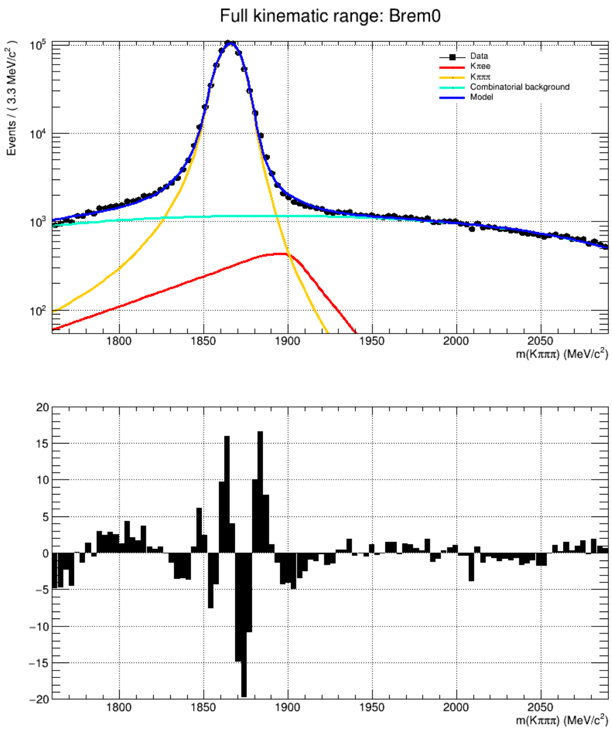

Figure 6.3: Data fit in the full kinematic range, Category Brem0. The fit is shown with a logarithmic y-scale. Pull plot is presented with larger y-scale.

List of Figures

List of Tables

Acknowledgments

Ich möchte die Gelegenheit nutzen, um mich bei einigen Menschen zu bedanken. Zunächst bei Daniel Unverzagt und Professor Uwer für die gute Betreuung und Unterstützung bei der Durchführung dieser Bachelorarbeit. Ein besonderer Dank gilt den Menschen, die mich in meinem Studium unterstützt haben. Dazu gehören meine Familie und all die Freunde die mich über die Jahre geprägt haben. Besonders erwähnen möchte ich die Menschen, die mit mir gemeinsam die Höhen und Tiefen des Physikstudiums durchlebt haben. Ohne euch wäre es sehr viel weniger schön gewesen.

Erklärung

Ich versichere, dass ich diese Arbeit selbstständig verfasst und keine anderen als die angegebenen Quellen und Hilfsmittel benutzt habe.

F. Linsenmeier

Heidelberg, den 01. August 2022